OPEN ACCESS

Energy Chemistry ARTICLE

The Innovation Energy

# Sustainable synthesis of NaA zeolite-modified $MnFe_2O_4$ for synergistic removal of $NH_4^+$ and tetracycline

Yesha Song,[1] Bangting Xu,[1] Xinyang Bao,[1] Yi Yu,[1] Qi Zhang,[1] Kaixiang Ren,[1] Wenjie Weng,[1] Yuwei Zhou,[1] Shenxuan Yuan,[1] Siying He,[1] Yaohui Hu,[1] Dazhi Jin,[1,3,4,*] and Yulei Tai[1,2,4,*]

*Correspondence: taiyulei@163.com (Y. T.); jind@hmc.edu.cn (D. J.)

Received: November 30, 2025; Accepted: April 17, 2026; Published Online: April 20, 2026; https://doi.org/10.59717/j.xinn-energy.2026.100151



## GRAPHICAL ABSTRACT

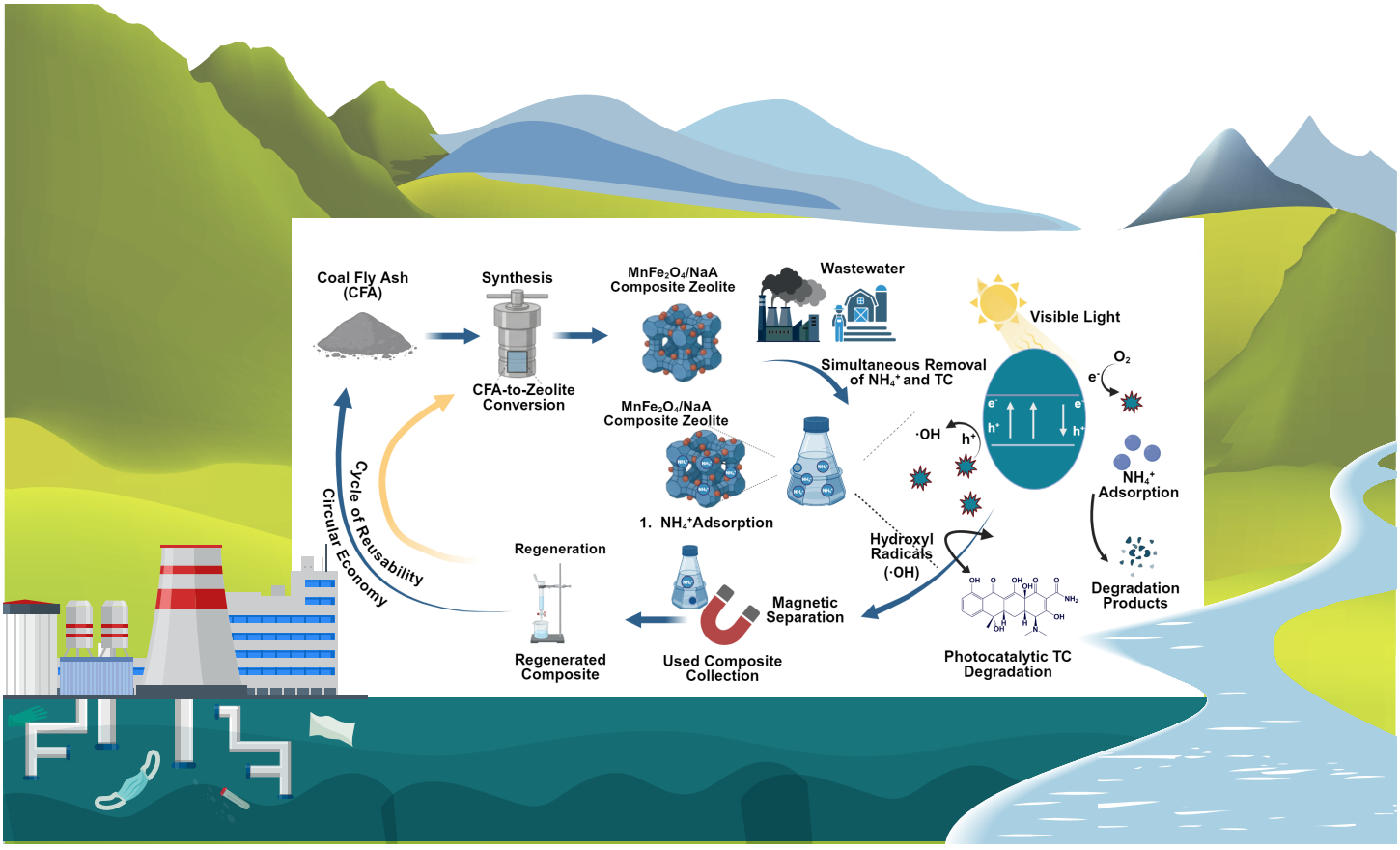


## PUBLIC SUMMARY

- Coal fly ash is converted into a $MnFe_2O_4$/NaA composite for sustainable wastewater treatment.
- The material removes ammonium ($NH_4^+$-N) and degrades tetracycline simultaneously.
- Adsorption and photocatalysis work together to enhance pollutant removal efficiency.
- The composite shows strong stability and can be reused multiple times.
- This approach supports circular economy by turning waste into high-value materials.

ARTICLE Energy Chemistry

OPEN ACCESS

# Sustainable synthesis of NaA zeolite-modified $MnFe_2O_4$ for synergistic removal of $NH_4^+$ and tetracycline

Yesha Song,[1] Bangting Xu,[1] Xinyang Bao,[1] Yi Yu,[1] Qi Zhang,[1] Kaixiang Ren,[1] Wenjie Weng,[1] Yuwei Zhou,[1] Shenxuan Yuan,[1] Siying He,[1] Yaohui Hu,[1] Dazhi Jin,[1,3,4,*] and Yulei Tai[1,2,4,*]

[1]Hangzhou Medical College, Hangzhou 310053, China

[2]School of Medicine, Hangzhou Medical College, Hangzhou 310053, China

[3]Laboratory of Biomarkers and In Vitro Diagnosis Translation of Zhejiang Province, Hangzhou 310000, China

[4]Department of clinical laboratory, Zhejiang Provincial People's Hospital, Hangzhou Medical College, Hangzhou 310053, China

*Correspondence: taiyulei@163.com (Y. T.); jind@hmc.edu.cn (D. J.)

Received: November 30, 2025; Accepted: April 17, 2026; Published Online: April 20, 2026; https://doi.org/10.59717/j.xinn-energy.2026.100151



Citation: Song Y., Xu B., Bao X., et al. (2026). Sustainable synthesis of NaA zeolite-modified $MnFe_2O_4$ for synergistic removal of $NH_4^+$ and tetracycline. *The Innovation Energy* 3:100151.

A sustainable hydrothermal strategy converts coal fly ash, an industrial byproduct, into $MnFe_2O_4$/NaA composite molecular sieves. Despite the promise of molecular sieve-based composites in water remediation, existing materials often lack sufficient recyclability, long-term stability, and a clear understanding of their regeneration mechanisms. This approach addresses these knowledge gaps and waste management while creating a material capable of simultaneously removing $NH_4^+$-N and photo-catalytically degrading tetracycline (TC). The composite demonstrates synergistic pollutant removal via integrated adsorption-photocatalysis. Comprehensive characterization confirmed the successful integration of $MnFe_2O_4$ nanoparticles within the NaA framework. The optimized 8% $MnFe_2O_4$/NaA composite achieved exceptional performance, with 66% $NH_4^+$-N removal and 89% TC degradation under optimal conditions. The processes followed pseudo-second-order kinetics, and radical trapping identified •OH as the dominant reactive species. Remarkably, the composite maintained high efficiency across multiple regeneration cycles, demonstrating robust stability and reusability. This work presents a novel, waste-derived material that aligns with circular economy principles by transforming fly ash into a high-value adsorbent/catalyst for wastewater treatment.

## INTRODUCTION

With the rapid development of the livestock and poultry industry, ammonia nitrogen ($NH_3$) and tetracycline (TC) have become major contributors to aquatic pollution.[1] Studies reveal that over 70% of TC is excreted as unmetabolized parent compounds or metabolites through feces,[2-4] while excessive ammonia nitrogen and antibiotic residues propagate through the food chain, posing risks to human health and ecosystems.[5-7] The development of high-value-added applications for coal combustion-derived fly ash presents a promising strategy for sustainable waste management and environmental remediation,[8] aligning with circular economy principles to mitigate pollution associated with coal-based industrial byproducts.[9] Hydrothermal and alkali fusion methods have been employed to synthesize fly ash-based zeolite molecular sieves,[10] demonstrating exceptional performance in ammonia nitrogen adsorption and TC degradation.[11] For instance, NaA/NaX dual-phase zeolites achieved a 90% ammonia nitrogen removal rate,[12-14] and $TiO_2$-loaded MCM-41 effectively enhanced TC photocatalytic efficiency.[15,16] Furthermore, $MnFe_2O_4$/NaA molecular sieves synergistically combined adsorption and photocatalysis, attaining 66% ammonia nitrogen removal and 89% TC degradation (this study). These advancements not only mitigate fly ash accumulation but also provide sustainable strategies for treating wastewater containing ammonia nitrogen and antibiotics, aligning environmental remediation with economic benefits.[17]

In recent years, molecular sieves have demonstrated significant potential in water pollution remediation.[18] However, while molecular sieve-based composites show promise for water remediation, significant challenges limit their practical use.[8] Many existing materials lack sufficient recyclability and long-term stability.[19] Additionally, there is a recognized need for research focused on optimizing both adsorption and catalytic functions within a single material to improve overall treatment efficiency.[20] Moreover, a key mechanistic gap exists, as future studies should aim to clarify the fundamental mechanisms behind regeneration processes to support robust and sustainable implementation.[21] Enhanced both adsorption and photocatalytic performance by modifying ZSM-5 molecular sieves with $Fe^{3+}$ for efficient methyl orange degradation via a photocatalytic Fenton reaction.[22] Immobilized $TiO_2$ nanoparticles on molecular sieves, achieving over 90% degradation of rhodamine B under visible light while improving catalyst dispersion and stability.[23] Further developed a composite by loading MCM-41 and $TiO_2$ onto molecular sieves, effectively degrading tetracycline. However, insufficient recyclability and long-term stability hinder their practical applications,[24] necessitating research on synergistic optimization of adsorption and catalytic functions.[25] Photocatalytic technology has emerged as an environmentally benign strategy with significant potential for sustainable energy applications. The immobilization of transition metal oxides (e.g., $MnFe_2O_4$) on molecular sieve substrates effectively improves active site distribution and facilitates radical formation,[26] thereby achieving enhanced degradation efficiency of antibiotic compounds. Studies indicate that regulating the pore structure and surface properties of molecular sieves is critical.[27] Subsequent research should prioritize elucidating the fundamental mechanisms underlying regeneration processes while concurrently advancing scalable implementations to enable effective translation into practical wastewater treatment systems.[28]

Photocatalytic technology has gained increasing attention as a promising strategy for sustainable wastewater remediation, owing to its inherent advantages including cost-effectiveness, low energy requirements, and environmental compatibility. In light-driven Fenton processes, photocatalysts play a pivotal role in enhancing catalytic activity.[29] Spinel-type manganese ferrite ($MnFe_2O_4$) has garnered significant attention due to its exceptional performance in photocatalytic Fenton reactions. It efficiently decomposes $H_2O_2$ to generate reactive oxygen species (e.g.,·OH,·$O_2^-$), enabling effective degradation of organic pollutants.[30,31] Compared to $CoFe_2O_4$, which tends to release toxic $Co^{2+}$ ions, and $NiFe_2O_4$ with insufficient catalytic performance, $MnFe_2O_4$ combines environmental safety with superior catalytic efficiency.[32] Moreover, the exceptional stability and robust recyclability of the system contribute to a substantial reduction in operational expenditures. However, the intrinsic strong magnetic properties of $MnFe_2O_4$ tend to induce undesirable particle aggregation, which in turn compromises photon utilization efficiency and poses a major challenge for its practical implementation.[27] Addressing this challenge requires developing simple yet effective strategies to improve dispersion and photocatalytic activity.[33] For instance, strategies such as carrier loading or morphological modification can optimize the separation efficiency of photogenerated charge carriers, thereby overcoming performance limitations and facilitating practical applications in wastewater treatment.

While molecular sieve-based composites show promise for water remediation, significant challenges limit their practical use. Many existing materials lack sufficient recyclability and long-term stability. Additionally, there is a recognized need for research focused on optimizing both adsorption and catalytic functions within a single material to improve overall treatment efficiency. Moreover, a key mechanistic gap exists, as future studies should aim to clarify the fundamental mechanisms behind regeneration processes to support robust and sustainable implementation. In this study, we report the preparation of $MnFe_2O_4$/NaA zeolite composite from coal fly ash using a hydrothermal method for simultaneous NH3 adsorption and TC photocatalytic degradation. Structural characterization (XRD, SEM, XPS) confirmed its crystallinity and morphology. Under optimal conditions (1.6 g·$L^{-1}$ dosage, 50 mM $H_2O_2$, pH 7), 8% $MnFe_2O_4$/NaA achieved 66% $NH_3$ removal and 89%

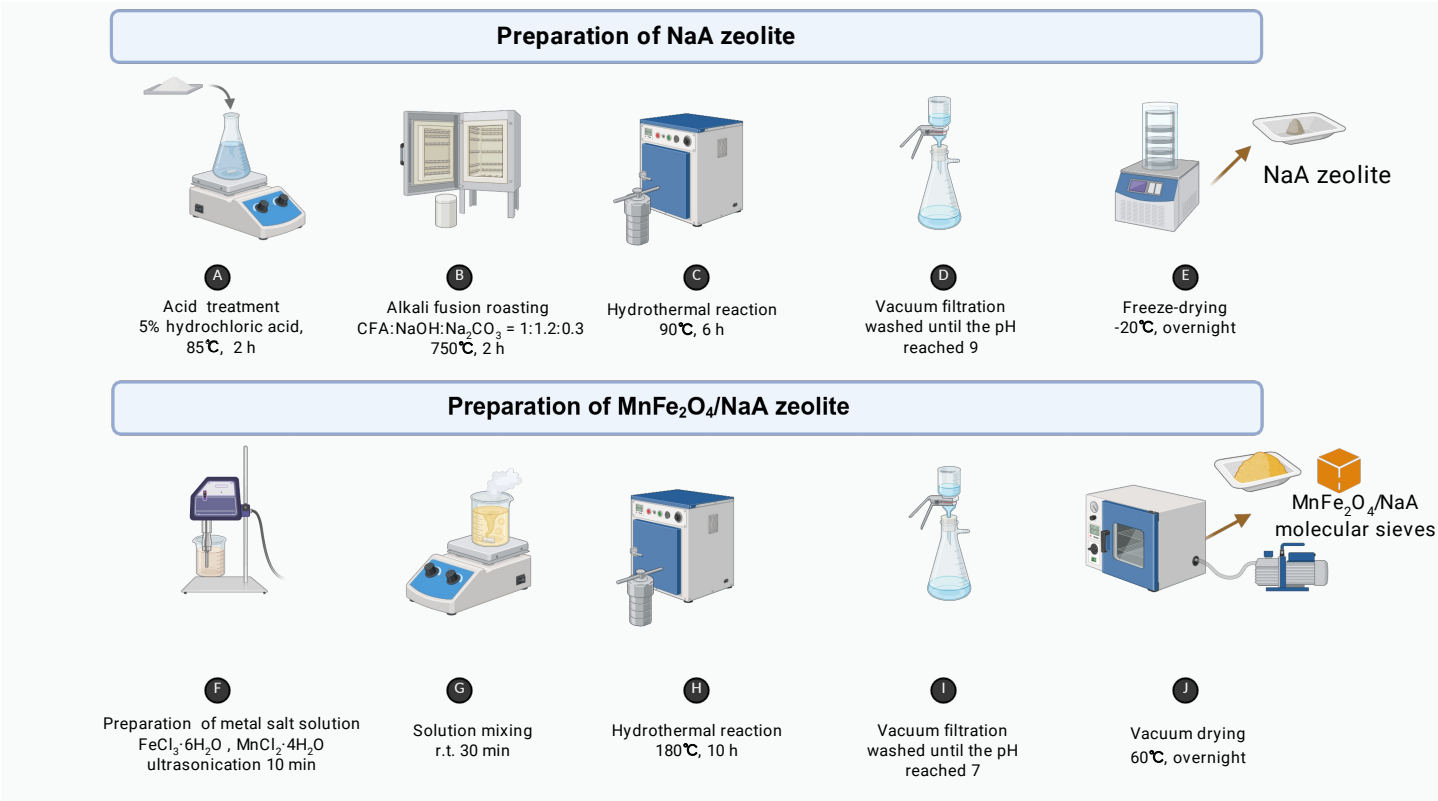


**Figure 1. Flow chart for the preparation of $MnFe_2O_4$/NaA molecular sieves**

TC degradation. After four regeneration cycles, efficiencies remained at 64% ($NH_3$) and 67% (TC). This material demonstrates high adsorption capacity, catalytic activity, and recyclability, offering a sustainable solution for antibiotic-contaminated wastewater.

## MATERIALS AND METHODS

### Material

Sodium metasilicate pentahydrate ($Na_2SiO_3{\cdot}5H_2O$), ammonium chloride ($NH_4Cl$), manganese(II) nitrate tetrahydrate ($Mn(NO_3)_2{\cdot}4H_2O$), sodium potassium tartrate tetrahydrate ($C_4H_4O_6KNa{\cdot}4H_2O$), cetyltrimethylammonium bromide ($C_{19}H_{42}BrN$, CTAB), ferric chloride hexahydrate ($FeCl_3{\cdot}6H_2O$), and manganese(II) chloride tetrahydrate ($MnCl_2{\cdot}4H_2O$) were all purchased from Shanghai Macklin Biochemical Technology Co. Ltd. Potassium tetraiodomercurate(II) ($K_2(HgI_4)$) and ferric chloride nonahydrate ($FeCl_3{\cdot}9H_2O$), as well as tetracycline hydrochloride ($C_{22}H_{24}N_2O_8{\cdot}HCl$, TC), were obtained from Shanghai Aladdin Bio-Chem Technology Co. Ltd.

### Preparation of $MnFe_2O_4$/NaA zeolite

Synthesize NaA zeolite.[34] Firstly, coal fly ash was treated with 5% hydrochloric acid at a liquid-to-solid ratio of 20%. The mixture was heated to 85°C and stirred magnetically for 2 hours, then washed and dried for further use. A pre-treated fly ash sample weighing 5.00 g was taken, and the mass ratio of fluxes was adjusted to CFA:NaOH:$Na_2CO_3$ = 1:1.2:0.3. The sample was then calcined at 750°C for 2 hours, cooled to room temperature, and subsequently ground. Another 5.00 g of the alkali fusion product was taken and mixed with 2.9 mmol of $Na_2SiO_3{\cdot}5H_2O$ to achieve a silica-alumina ratio (Si/Al) of CTAB (2.22 g) was added, followed by the addition of 47 mL of deionized water to obtain a liquid-to-solid ratio of 6. The mixture was subjected to a hydrothermal reaction at 90°C for 6 hours. After completion of the reaction, the product was cooled, filtered, and washed until the pH reached 9. Subsequently, the product was placed in a -20°C freezer and stored for 2 hours before undergoing freeze-drying overnight. After grinding, the product was calcined at 500°C for 2 hours to remove CTAB, resulting in the formation of NaA-type zeolite.[35]

12 mmol of $FeCl_3{\cdot}6H_2O$ and 12.7 mmol of $MnCl_2{\cdot}4H_2O$ were separately dissolved in 15 mL of deionized water. The prepared NaA zeolite powder was dispersed in 10 mL of deionized water by ultrasonication for 10 minutes. The $MnCl_2{\cdot}4H_2O$ solution was poured into the $FeCl_3{\cdot}6H_2O$ solution to form solution A. The zeolite solution was dropwise added to solution A using an autosampler and stirred to obtain solution B. 10mL 8M NaOH was then added drop by drop to solution B using an autosampler, followed by vigorous stirring on a magnetic stirrer for 30 minutes to obtain a suspension. Finally, approximately 50 mL of the mixed solution was transferred to a 100 mL autoclave and subjected to hydrothermal treatment at 180°C for 10 hours in an oven. After synthesis, the autoclave was cooled and removed from the oven. The aqueous nanoscale particle suspension formed was separated using an external magnet. It was washed repeatedly three times with deionized water and anhydrous ethanol. Lastly, it was dried overnight in an oven at 60°C. In this study, $MnFe_2O_4$/NaA zeolite with varying NaA mass ratios (4.0 wt%, 6.0 wt%, 8.0 wt%, 10.0 wt%, 15.0 wt%, and 20.0 wt%) is prepared.

### Characterization

The phase purity and crystal structure of were investigated using an X-ray diffractometer (XRD, X'Pert PRO MPD). The lattice properties and morphology of the prepared samples were characterized using a scanning electron microscope (SEM, Zeiss Sigma 300). Moreover, X-ray photoelectron spectroscopy (XPS, Thermo K-Alpha) was employed to study the surface chemical states of the unprepared samples. Furthermore, the mass changes of the samples during the heating process were studied using a thermogravimetric analyzer (TGA, TG-DTA8122) to understand their thermal stability and decomposition behavior. The magnetic properties of the samples, including magnetization curves, coercivity, and magnetic susceptibility, were investigated using a vibrating sample magnetometer (VSM, LakeShore7404) to reveal the magnetic behaviors and properties of the zeolite.

### Adsorption of ammonia nitrogen($NH_4^+$-N)

3.819 g of $NH_4Cl$ was dissolved in deionized water to obtain a 1000 mg·$L^{-1}$ ammonia nitrogen stock solution. This solution was further diluted to prepare a 40 mg·$L^{-1}$ ammonia nitrogen solution, which was then used to prepare a 20 mg·$L^{-1}$ TC mixed ammonia nitrogen solution. 50 mg $MnFe_2O_4$/NaA, dried under vacuum at 65°C for 1 h, was added to 50 mL of the mixed solution. The mixture was oscillated at 25°C with a frequency of 150 r·$min^{-1}$ for 15 min.

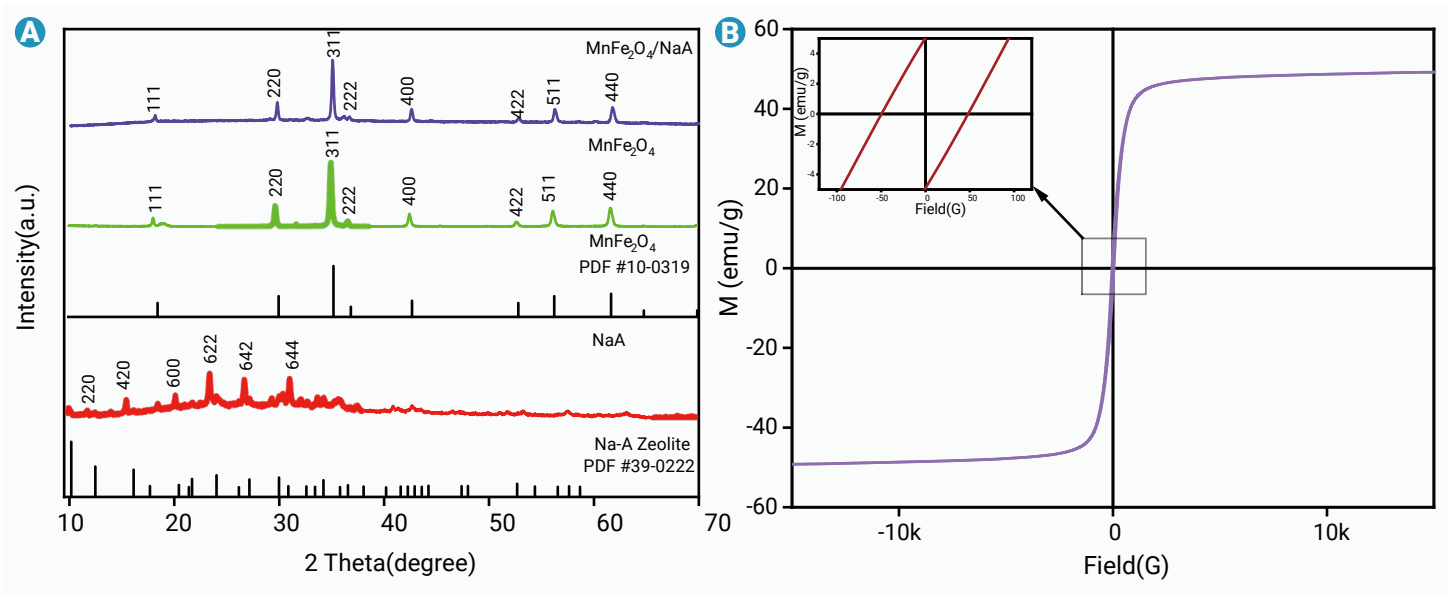


**Figure 2. (A) XRD patterns of NaA, $MnFe_2O_4$ and 8% $MnFe_2O_4$/NaA; (B) VSM spectrum of 8% $MnFe_2O_4$/NaA**

Afterward, 3 mL of the supernatant was withdrawn and filtered through a 0.45 μm disposable membrane into a 25 mL colorimetric tube. Then, 1 mL of 1.78 M masking agent sodium potassium tartrate, and 1 mL of color reagent Nessler's reagent were added, and the volume was adjusted to 25 mL. After standing for 10 min, the absorbance of the solution at 420 nm wavelength was measured using a UV-visible spectrophotometer. The ammonia nitrogen content in the solution was determined based on the linear fitting equation of the ammonia nitrogen standard curve. Each experiment was conducted in triplicate, and the average value was used for further analysis. In this study, $C_t$ represents the concentration of ammonia nitrogen in the solution at time t, $C_0$ is the initial concentration of ammonia nitrogen in the solution, and $C_t/C_0$ indicates the ratio of ammonia nitrogen concentration at a given time point to the initial concentration, reflecting the change in ammonia nitrogen concentration over time.

### Photo-Fenton degradation of TC

The catalytic activity of the prepared catalyst was evaluated by assessing the degradation of TC in the presence of $H_2O_2$ under visible light irradiation. 50 mg $MnFe_2O_4$/NaA zeolite was added to a 30 mL mixed solution and sonicated for 3 min to ensure complete dispersion of the sample. Subsequently, the suspension was mechanically stirred (150 r·min$^{-1}$) in the dark for 30 min to establish adsorption-desorption equilibrium. Then, 3% $H_2O_2$ was added dropwise to the mixed solution to achieve a concentration of 50 mM. During the visible light irradiation process, 3 mL of the suspension was extracted at known intervals and filtered through a disposable membrane with a pore size of 0.45 μm. Control experiments were conducted under the same conditions using NaA zeolite and $MnFe_2O_4$ separately. The remaining concentration of TC was monitored by measuring its characteristic absorbance at 357 nm wavelength using a UV-visible spectrophotometer. Each experiment was performed in triplicate, and the average values obtained were further analyzed. Similar to the former, $C_t$ represents the TC concentration in the solution at time t, $C_0$ denotes the initial concentration of TC in the solution, and $C_t/C_0$ indicates the ratio of TC concentration at a specific time point to the initial concentration, which is used to track the changes in TC concentration over time. In addition, the contribution of ROS in the $MnFe_2O_4$/NaA zeolite/TC system was determined.[36] Isopropanol (IPA), p-Benzoquinone (p-BQ), and disodium ethylenediaminetetraacetate (EDTA-2Na) were exploited as scavengers to rapidly quench ·OH, $O_2^-$, and holes ($h^+$), respectively.[37]

## Results and discussion

### Characterizations

XRD was employed to identify the crystallographic information and purity of the prepared materials. The XRD results of NaA zeolite, $MnFe_2O_4$, and 8%$MnFe_2O_4$/NaA zeolite are illustrated in Figure 2A. The diffraction peaks observed at 10.18° (220), 16.13° (420), 23.48° (622), 26.82° (642), and 31.12° (644) correspond to the main crystal phase of NaA zeolite (PDF#39-0222), indicating the successful synthesis of NaA zeolite.[38] However, the peak positions of the synthesized material may shift, typically due to slight variations in lattice parameters arising from impurities introduced during synthesis, ion exchange, or structural stress. Additionally, the broadening of the peaks is mainly due to a reduction in crystallite size. According to the Scherrer equation, the full width at half maximum of diffraction peaks is inversely proportional to the crystallite size.[39] Similarly, the diffraction peaks observed at 18.1° (111), 29.74° (220), 35.02° (311), 36.62° (222), 42.52° (400), 52.74° (422), 56.18° (511), and 61.68° (440) match the main crystal phase of $MnFe_2O_4$ (PDF#10-0319), demonstrating the successful preparation of $MnFe_2O_4$. Moreover, a characteristic diffraction peak of NaA zeolite was observed at 2θ=32.58°, indicating the successful loading of $MnFe_2O_4$ onto the surface of NaA zeolite. However, no other prominent diffraction peaks corresponding to NaA zeolite were observed in the 8% $MnFe_2O_4$/NaA zeolite material, which may be attributed to the lower content of NaA zeolite and subsequently lower intensity of its characteristic peaks. Furthermore, the absence of other impurity peaks indicates the high purity of the prepared materials. The XRD pattern of the catalyst after four consecutive adsorption-degradation cycles confirms the retention of the characteristic diffraction peaks for both the NaA zeolite framework and the $MnFe_2O_4$ spinel phase, indicating that the core composite structure remains intact. However, a noticeable decrease in peak intensity along with slight broadening is observed. These changes can be attributed to factors such as partial amorphization, surface restructuring, or the adsorption of reaction intermediates and byproducts on the catalyst surface, which is consistent with the gradual decline in tetracycline degradation efficiency observed over multiple cycles. Meanwhile, the magnetic properties of 8%$MnFe_2O_4$/NaA zeolite were characterized using VSM (Figure 2B). It can be observed that the magnetic hysteresis loop of the prepared zeolite exhibits a typical S-shaped curve, reaching a saturation magnetization of 49.23 emu/g at 15 G, which is lower than the saturation magnetization of pure $MnFe_2O_4$ bulk (80.00 emu/g), further confirming the successful loading of $MnFe_2O_4$ on NaA zeolite. Moreover, based on the data, the remanence and coercivity of 8% $MnFe_2O_4$/NaA zeolite are measured to be 5.12 emu/g and 47.74 Oe, respectively, indicating a superparamagnetic behavior. The coercivity (Hc) value of approximately 0 Oe, as indicated by the VSM analysis, is a characteristic feature of superparamagnetic behavior. This property arises because the $MnFe_2O_4$ nanoparticles in our composite have a size below the critical single-domain threshold (typically < 20-30 nm for ferrites). At this scale, each nanoparticle acts as a single magnetic domain, and the thermal energy at room temperature is sufficient to overcome the magnetic anisotropy energy

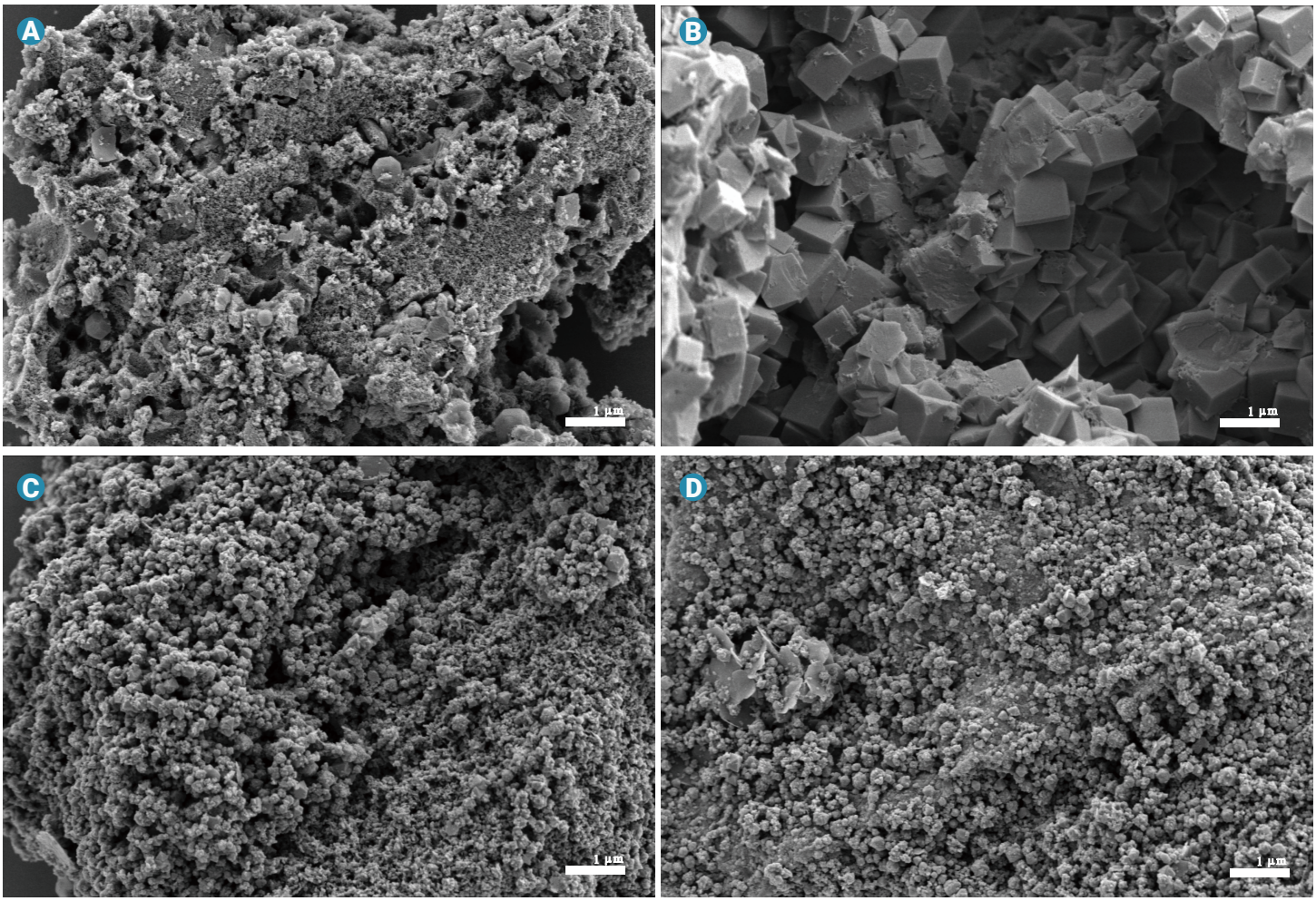


**Figure 3. (A) SEM images of $MnFe_2O_4$; (B) NaA; (C) 8% $MnFe_2O_4$/NaA; (D) 8% $MnFe_2O_4$/NaA (used after 4 cycles )**

barrier. This causes the magnetic moments to fluctuate randomly in the absence of an external field, resulting in zero net remanent magnetization and coercivity on the measurement timescale.[40,41] Similar superparamagnetic behavior has been specifically reported for hydrothermally synthesized $MnFe_2O_4$ nanoparticles of around 9 nm in size.[42] This characteristic is advantageous for dispersing zeolite in solution while retaining magnetic properties for separation.

As shown in Figure 3A, $MnFe_2O_4$ exhibits an aggregated morphology with non-uniform size distribution. In contrast, NaA zeolite is composed of relatively regular cubic hexahedra with a larger volume (Figure 3B). A comparison between $MnFe_2O_4$ and NaA zeolite reveals that 8% $MnFe_2O_4$/NaA zeolite consists of uniformly sized microspheres and a small number of square stones (Figure 3C). Moreover, SEM images of the spent catalyst show that the composite's microcubic morphology is largely preserved, although some surface roughening and minor particle aggregation are evident compared to the fresh catalyst (Figure 3D). The particle size distribution of 8% $MnFe_2O_4$/NaA is more uniform, indicating successful NaA integration into $MnFe_2O_4$. The elemental composition corresponding to these morphologies has been confirmed by XRD and XPS analyses (see Figures 4 & 5).

The identification of specific chemical bonds and oxidation states through XPS analysis offers valuable information regarding the surface properties and reactivity of the composite, and the results are shown in Figure 4. In the $MnFe_2O_4$/NaA system, four elements—C, O, Mn, and Fe—are detected, with binding energy peaks primarily centered at 284.2, 529.6, 640.7, and 710.5 eV (Figure 4A). In the C 1s spectrum (Figure 4B), the peak was deconvoluted into two distinct components at 284.2 eV and 287.8 eV, corresponding to adventitious carbon (C-C/C=C) and oxygen-bound carbon (O-C=O), respectively. The high-resolution O 1s spectrum (Figure 4C) was properly separated into two distinct peaks. The prominent peak at 529.6 eV is assigned to the metal-oxygen (M-O) lattice oxygen ($O^{2-}$) within the $MnFe_2O_4$ spinel structure. A secondary deconvoluted peak at 531.1 eV corresponds to surface-adsorbed oxygen species or surface hydroxyl (-OH) groups, which act as vital reactive sites for catalytic interactions. While the peak at 531.1 eV may indicate adsorbed oxygen or surface hydroxyl groups on the composite material, suggesting potential reactive sites involved in surface reactions or interactions with other molecules. Furthermore, accurate peak deconvolution of the transition metals reveals their mixed valence states. The Mn 2p spectrum (Figure 4D) exhibits spin-orbit doublets Mn 2p3/2 and Mn 2p1/2. Through peak separation, the Mn 2p3/2 peak at 640.7 eV confirms that manganese primarily exists in the +2 oxidation state ($Mn^{2+}$). Similarly, the high-resolution Fe 2p spectrum (Figure 4E) was deconvoluted to separate the $Fe^{2+}$ and $Fe^{3+}$ contributions. The fitted peaks at 710.5 eV and 724.3 eV correspond to the Fe 2p3/2 and Fe 2p1/2 states, respectively. The presence of distinct satellite peaks separated out at 718.3–719.7 eV further corroborates the coexistence of $Fe^{2+}$ and $Fe^{3+}$ in the composite. The survey and high-resolution spectra (C 1s, O 1s, Mn 2p, Fe 2p) for both $MnFe_2O_4$ and the 8% $MnFe_2O_4$/NaA composite are normalized to their respective maximum peak intensities to facilitate a clear comparison of peak positions and shape. In conclusion, the XPS analysis confirms the successful formation of the $MnFe_2O_4$/NaA composite, detecting C, O, Mn, and Fe elements on its surface and indicating the presence of $Mn^{2+}$, $Fe^{2+}$, and $Fe^{3+}$, respectively.[27] This successful peak separation confirms the complex mixed-valence nature of the composite, which is a fundamental prerequisite for the efficient generation of reactive oxygen species during the Fenton-like photocatalytic process and potential catalytic functionality, both of which are crucial for the material's performance in pollutant-removal applications.

The presence of these elemental groups indicates interactions and activation processes between transition-metal atoms and $MnFe_2O_4$/NaA. The

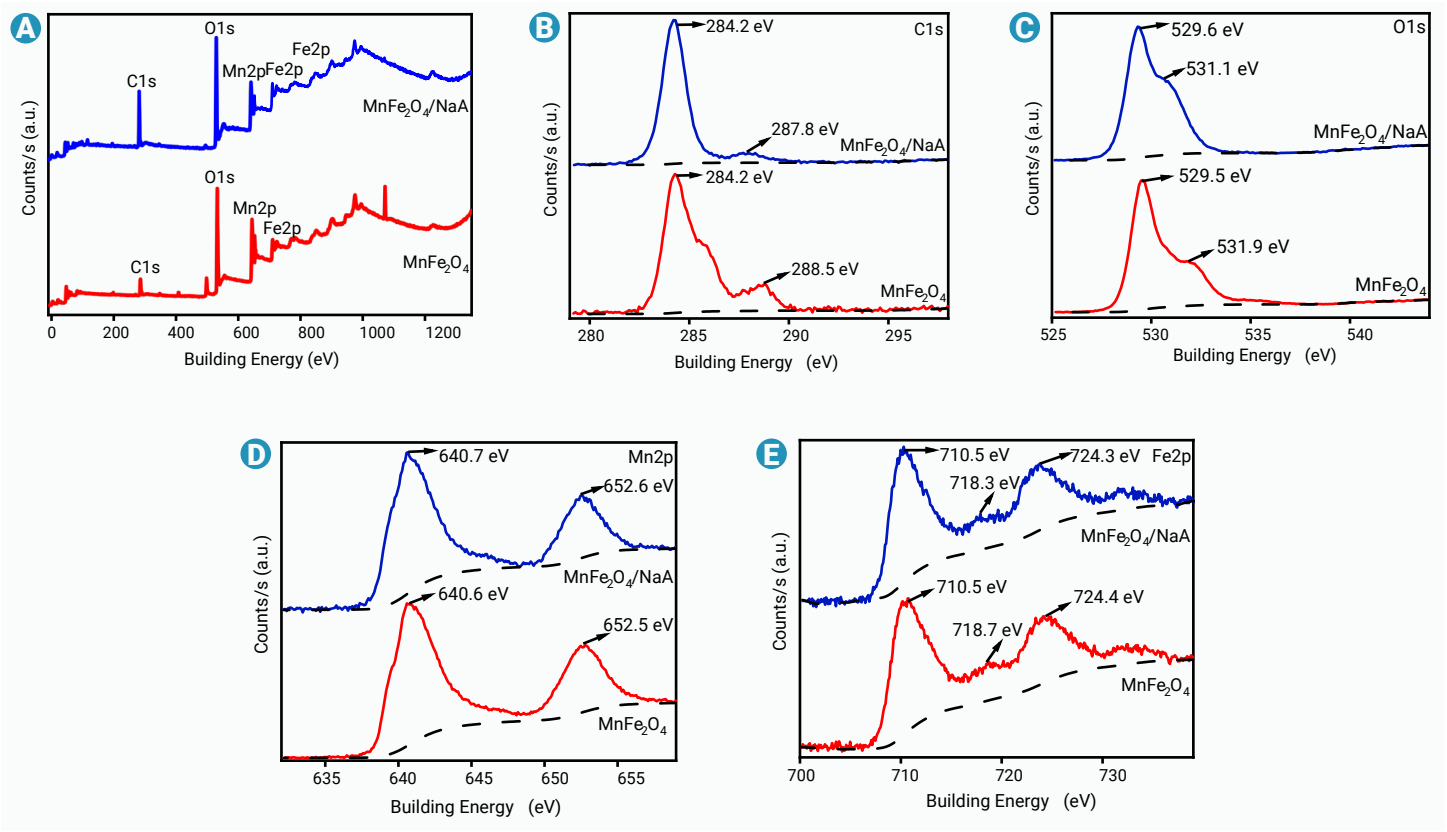


**Figure 4. XPS analysis of $MnFe_2O_4$ and 8% $MnFe_2O_4$/NaA** (A) XPS survey spectra of $MnFe_2O_4$ and 8% $MnFe_2O_4$/NaA; (B) C 1s; (C) O 1s; (D) Mn 2p; (E) Fe 2p

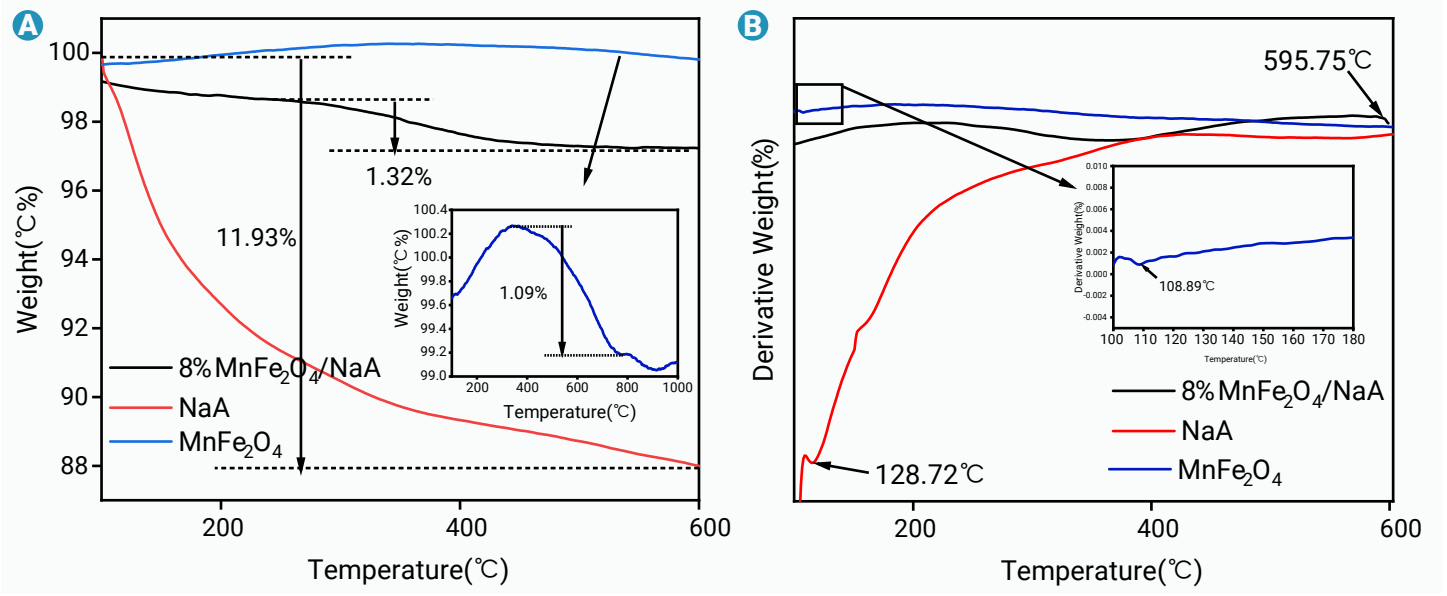


**Figure 5. Curves of $MnFe_2O_4$, NaA and 8% $MnFe_2O_4$** (A) TGA; (B) DTG. Over as-prepared samples with different content of NaA.

detection of carbon species associated with different bonding configurations, along with the characterization of manganese and iron in distinct oxidation states, points towards the complex nature of the $MnFe_2O_4$/NaA system. The coexistence of multiple oxidation states suggests redox activities and potential catalytic functionalities of the composite material, which could be crucial for various applications such as catalysis, adsorption, or environmental remediation.

Thermogravimetric analysis (TGA) and differential thermogravimetric analysis (DTG) are important tools in thermal analysis techniques. By measuring changes in a substance's mass with temperature, as well as the exothermic or endothermic reactions, we can gain insights into thermal stability, thermal decomposition processes, and other thermal properties of materials. Figure 5 presents the TGA and DTG curves of NaA, $MnFe_2O_4$, and 8% $MnFe_2O_4$/NaA zeolite. From the TGA curve in Figure 5A, it is observed that NaA zeolite continuously loses weight (12.14%) with increasing temperature, while the 8% $MnFe_2O_4$/NaA zeolite exhibits a much lower weight loss of only 2.57%. This difference can be attributed to the significant loss of physically adsorbed water in NaA zeolite, whereas the $MnFe_2O_4$/NaA zeolite shows less water adsorption due to its weaker pore structure. Conversely, the mass of $MnFe_2O_4$ exceeds 100%, indicating possible oxidation of $MnFe_2O_4$ at high tempera-

tures, leading to the formation of new compounds. Analyzing the DTG curves in Figure 5B, a peak at 128.72°C is observed for NaA zeolite, corresponding to a significant weight loss as water within the pores is desorbed upon heating. The weight loss peak of the 8% $MnFe_2O_4$/NaA zeolite (595.75°C) shifts towards lower temperatures compared to $MnFe_2O_4$, indicating successful incorporation of NaA zeolite into $MnFe_2O_4$. This shift suggests interactions among the components, potentially influencing the composite material's thermal stability and decomposition behavior.[43] The derivative thermogravimetric (DTG) analysis reveals two distinct stages of mass loss. The first stage, occurring between 30 and 200 °C with a mass loss of approximately 9.5%, is attributed to the evaporation of physically adsorbed water. In contrast, a more significant mass loss of about 12.8% is observed in the temperature range of 200～800 °C, which corresponds to the decomposition of the zeolite framework and the phase transformation of the $MnFe_2O_4$ nanoparticles.

## Performance of adsorption of ammonia nitrogen and photocatalytic degradation of TC

At room temperature, the performance of adsorption of ammonia nitrogen and photocatalytic degradation of tetracycline (TC) under visible light irradiation using ammonium chloride and tetracycline hydrochloride as contaminants was evaluated, with the results depicted in Figure 5 C & D. In Figure 5C, compared to pure NaA zeolite, the adsorption rate of ammonia nitrogen by $MnFe_2O_4$/NaA zeolite generally decreased. This could be attributed to a reduction in the proportion of NaA zeolite at the same mass, and the weaker adsorption capacity of ammonia nitrogen by $MnFe_2O_4$, leading to subsequently decrease in its ability to adsorb ammonia nitrogen. As the content of NaA zeolite increased from 4% to 8%, the adsorption performance of $MnFe_2O_4$/NaA gradually improved. Specifically, the 8% $MnFe_2O_4$/NaA exhibited the optimal removal efficiency for ammonia nitrogen, reaching 51% removal after 90 minutes, compared to only an approximately 8% decrease with NaA zeolite alone. This enhancement may be attributed to the uniform dispersion of 8% NaA in $MnFe_2O_4$, providing sufficient contact points for effective adsorption. However, when the NaA content was further increased from 8% to 20%, the removal efficiency of ammonia nitrogen decreased.One possible explanation for the decrease in removal efficiency at higher NaA content is that excessive NaA could lead to pore blockage or hinder the access to active sites, thereby reducing the adsorption capacity. Moreover, at higher NaA content, the physical and chemical interactions at the interface between $MnFe_2O_4$ and NaA may change, affecting the overall adsorption performance. Moreover, an excess of NaA may cause aggregation or agglomeration, reducing the available effective surface area for adsorption.

In the context of photocatalytic degradation performance (Figure 5D), the pristine NaA zeolite exhibited the lowest efficiency. With the increase in NaA content from 4% to 8%, its capability for catalytic degradation of TC progressively escalated, reaching an optimal performance at 8% NaA with a degradation efficiency of 90%. This enhancement can be attributed to the ability of $MnFe_2O_4$ in the 8% $MnFe_2O_4$/NaA composite to provide sufficient catalytic active sites, while 8% NaA concurrently preserved the zeolite's pore structure and surface properties, which are conducive to the separation and utilization of electrons and holes, thereby enhancing the photocatalytic degradation performance. However, upon further increasing the NaA content, as with the adsorption of ammonia nitrogen, a decline in catalytic performance was observed. This phenomenon could be ascribed to an excess of NaA, which causes pore blockage, impeding the ingress of reactants to active sites and disrupting the electron-hole separation process, consequently diminishing the efficiency of photocatalytic degradation.

Furthermore, to examine the reaction kinetics of ammonia nitrogen adsorption and the photocatalytic degradation of TC on the modified zeolite, three kinetic models were used to fit the data from 8% $MnFe_2O_4$/NaA zeolite, with the equations shown in Equations (1) - (3). The results, shown in Figure 5 E & F, indicated that for both ammonia nitrogen adsorption and TC photocatalytic degradation, the pseudo-second-order model had the highest correlation coefficients, with $R^2$ values of 0.99739 and 0.99611. This shows that the pseudo-second-order model more accurately describes the processes of ammonia nitrogen adsorption and TC degradation, suggesting that $MnFe_2O_4$/NaA mainly promotes chemical adsorption of ammonia nitrogen. The differing final efficiencies (66% for $NH_4^+$-N and 89% for TC) arise because the removal of each pollutant is governed by entirely different mechanism. Ammonia nitrogen removal is primarily driven by chemical adsorption and ion-exchange processes facilitated by the zeolite framework. Conversely, tetracycline degradation is a photocatalytic process driven by the generation of reactive oxygen species (e.g., ·OH and $\cdot O_2^-$ radicals) under visible ligh. Because these pathways rely on different active sites and reaction kinetics, their respective removal capacities naturally differ. Based on recent literature from the past five years, we compared the goodness-of-fit ($R^2$) for several photocatalytic systems used to degrade tetracycline (TC). Most systems had $R^2$ values above 0.95, suggesting they follow the pseudo-first-order kinetic model well. Notably, the $SnO_2$/RGO composite achieved a very high $R^2$ of 0.9998,[40] showing its degradation pattern closely matches the model. This indicates that the reaction rate under light is consistent and predictable. Conversely, the GO-HAp system had a slightly lower $R^2$ of 0.95,[41] which could be due to its higher adsorption capacity or fluctuations in light intensity, but it still falls within a high fit range. Overall, these findings support the high efficiency and reproducibility of photocatalytic tetracycline degradation and lay a solid foundation for further mechanistic studies, such as reactive oxygen species trapping experiments.

$$q_t = q_e[1 - exp(-k_1 t)] \quad (1)$$

$$q_t = \frac{k_2 q_e^2 t}{1 + k_2 q_e t} \quad (2)$$

$$q_t = \frac{1}{b} ln(at + 1) \quad (3)$$

## Effects of various factors on the performance of photocatalytic degradation of TC

The concentration of catalyst $H_2O_2$, the pH of the catalytic environment, the concentration of TC, and the dosage of $MnFe_2O_4$/NaA zeolite are all crucial factors influencing the performance of photocatalytic degradation, as illustrated in Figure 6. As depicted in Figure 6A, the photocatalytic degradation efficiency increases from 63% to 73% as the $H_2O_2$ concentration escalates from 10 mM to 50 mM. However, the degradation efficiency at 50 mM $H_2O_2$ is lower than that at 50 mM, which may be attributed to the excessive $H_2O_2$ undergoing self-decomposition to form $H_2O$ and $O_2$, concurrently quenching the generated ·OH radicals and hence diminishing the catalytic degradation performance of TC.[44] Investigating the impact of the catalytic environment's pH, as shown in Figure 6B, reveals that the highest catalytic efficiency is achieved under neutral conditions(pH=7). With an increase in pH, the degradation efficiency of 8% $MnFe_2O_4$/NaA zeolite expressesively decreases. In complex real water matrices, these concentration-dependent effects collectively determine the overall removal efficiency, as common anions compete with target pollutants for active sites. Especially under acidic conditions (pH=3), $Cl^-$ from HCl occupies surface active sites and hampers the Fenton-like reaction. Additionally, certain anions scavenge reactive oxygen species (e.g., ·OH), reducing their availability for breaking down pollutants; at around pH=3, for example, Cl- reacts with ·OH to produce less reactive ·Cl and OH-, a mechanism also seen with common aquatic anions like $CO_3^{2-}$ and $NO_3^-$. Moreover, high levels of $PO_4^{3-}$ can bind with metal ions (e.g., Fe, Mn) on the catalyst surface, leading to leaching of active components or surface passivation. Interestingly, this observation contradicts the optimal acidic conditions for the Fenton reaction, especially since pH 3 should yield the best results. This discrepancy may stem from the influence of free radical reaction pathways within the system on the solution's pH. Under acidic conditions (pH=3), the introduction of $Cl^-$ into the system from hydrochloric acid occupies the catalyst's active sites, thereby impeding the Fenton reaction. Furthermore, it has been noted that around pH=3, $Cl^-$ can scavenge hydroxyl radicals to produce ·Cl and $OH^-$, which possesses lower oxidation capability. Conversely, under alkaline conditions (pH = 11), several factors alter the reaction pathways of free radicals. Firstly, $H_2O_2$ is unstable and prone to decomposition into $H_2O$ and $O_2$ at alkaline pH. Moreover, relatively inactive shuttle ions form at higher pH, thereby reducing $H_2O_2$ activity. Finally, high-valent iron

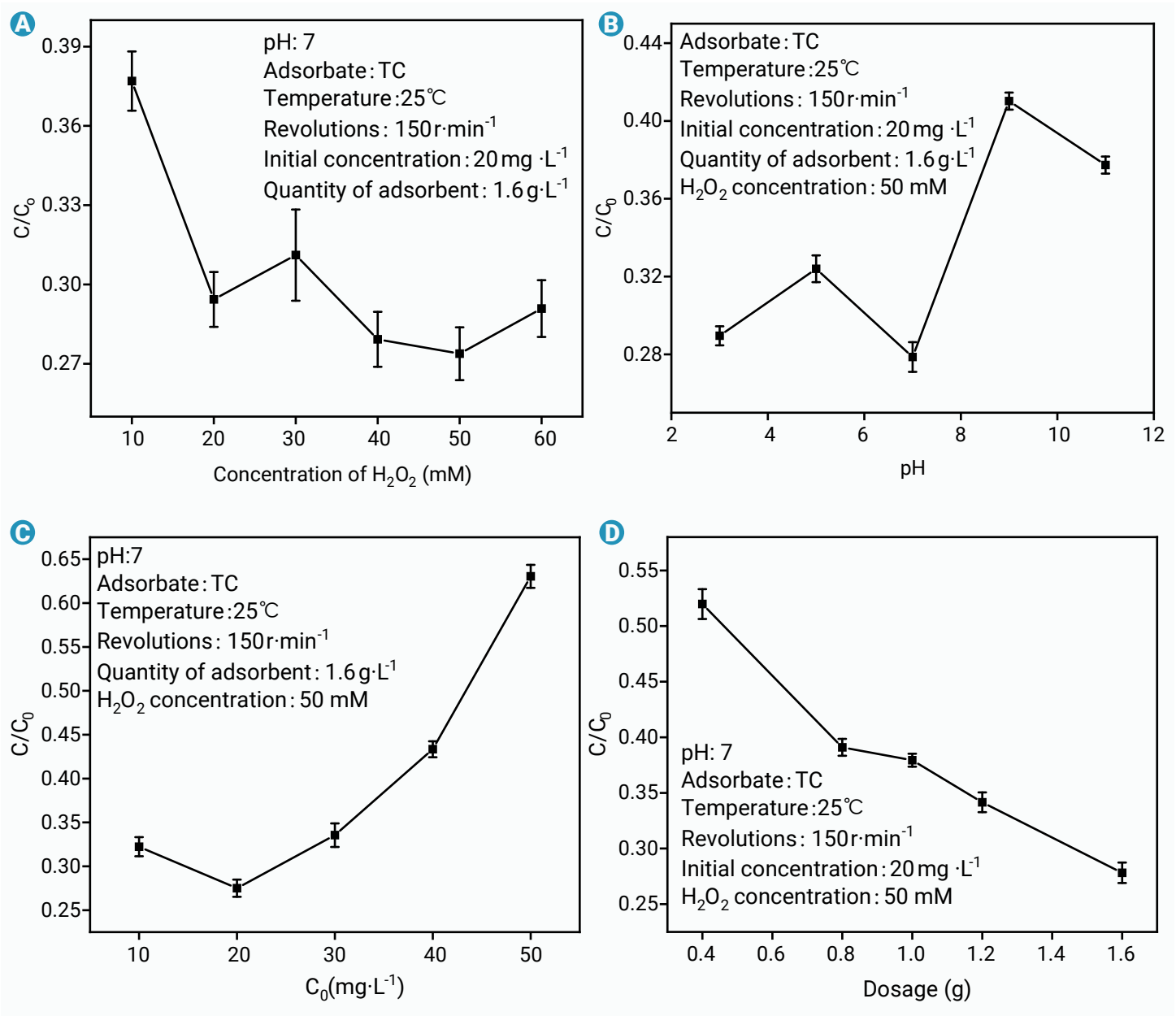


**Figure 6. 8%$MnFe_2O_4$/NaA on the performance of photocatalytic degradation of TC** (A) Effect of $H_2O_2$ concentration; (B) Effect of pH; (C) Effect of Initial TC concentration; (D) Effect of dosage

species ($Fe^{IV=0}$) may be generated under alkaline pH, which exhibit a lower redox potential compared to ·OH radicals. These effects arise through multiple concurrent mechanisms. Common anions compete with target pollutants (e.g., $NH_4^+$, TC) for active sites on the catalyst surface, especially under acidic conditions (pH=3), where $Cl^-$ from HCl occupies surface active sites and hampers the Fenton-like reaction. Additionally, certain anions scavenge reactive oxygen species (e.g., ·OH), reducing their availability for breaking down pollutants; at around pH=3, for example, $Cl^-$ reacts with ·OH to produce less reactive ·Cl and $OH^-$, a mechanism also seen with anions like $CO_3^{2-}$ and $NO_3^-$. Mo reover, the presence of ions influences the catalyst surface charge, affecting electrostatic interactions with ionic pollutants, while high levels of $PO_4^{3-}$ can bind with metal ions (e.g., Fe, Mn) on the catalyst surface, leading to leaching of active components or surface passivation. In the solution environment, anions such as $CO_3^{2-}$ can buffer local pH, which is crucial for reaction efficiency. Optimal degradation was observed at neutral pH in this study, and the ionic composition also impacts $H_2O_2$ stability. These concentration-dependent effects collectively determine the overall removal efficiency in complex water matrices.[45,46]

The degradation efficiencies at different initial concentrations are illustrated in Figure 6C, where it can be observed that the catalytic performance is optimal (73%) at an initial concentration of 20 mg·$L^{-1}$. As the initial concentration increases, the catalytic degradation efficiency gradually decreases. This phenomenon can be attributed to several factors. At higher concentrations, the active sites of the catalyst may become saturated, leading to a reduced interaction with the TC in the wastewater.

Moreover, more intermediate species may be generated during the reaction, competing for the adsorption of active species such as ·OH, thereby diminishing the efficiency of the catalytic degradation process. Reaction rates may also be influenced by mass transfer limitations, where the transfer of TC to the catalyst surface becomes a limiting factor in the overall reaction kinetics. However, the decrease in catalytic efficiency due to increasing concentrations can be addressed by extending the catalytic time. Finally, the impact of the dosage of $MnFe_2O_4$/NaA was investigated, with results depicted in Figure 6D. As the dosage increases from 0.4 g·$L^{-1}$ to 1.6 g·$L^{-1}$, the catalytic performance improves from 47% to 73%. This enhancement may be attributed to the provision of more active sites by a higher amount of catalyst, facilitating reactions with hydrogen peroxide to promote the generation of ·OH radicals and enhance degradation efficiency.

Table 1. Capacity comparison of selected materials to a host of deployed materials used for abatement of Tetracycline and $NH_4^+$-N.

| Material | Structure type | Synthesis Method | Target Pollutant | Efficiency(%) | Operating Conditions |
|---|---|---|---|---|---|
| This work (8% $MnFe_2O_4$/NaA) | NaA | One-pot hydrothermal | $NH_4^+$-N & TC (Simultaneous) | $NH_4^+$-N: 66%; TC: 89% | 25 °C, pH=7.00, 75min |
| $TiO_2$/MCM-41[15] | MCM-41 | Co-precipitation | Tetracycline | 91.80% | 25 °C, pH=6.80, 100min |
| V/Zn -MCM-41[16] | MCM-41 | Co-precipitation | Tetracycline | 98.13% | pH=5.10, 25min |
| $TiO_2$/ZnO[48] | ZSM-5 | Hydrothermal | $NH_4^+$-N | 73% | pH=9, 100min |
| Zeolite A[21] | Zeolite A | Impregnation | $NH_4^+$-N | 41.20% | 25 °C, pH = 6, 70min |
| Fe–60%$TiO_2$/BEA[22] | BEA Zeolite | Ion-exchange | Tetracycline | 80.1% | pH=1, 60min |
| $MnFe_2O_4$@HL [27] | Honey locust-derived carbon | Hydrothermal | Tetracycline | 92.7% | pH=3, 75min |
| $MnFe_2O_4$/ZIF-8[28] | ZIF-8 | Co-precipitation | Tetracycline | 90.2% | pH=3-11, 60min |

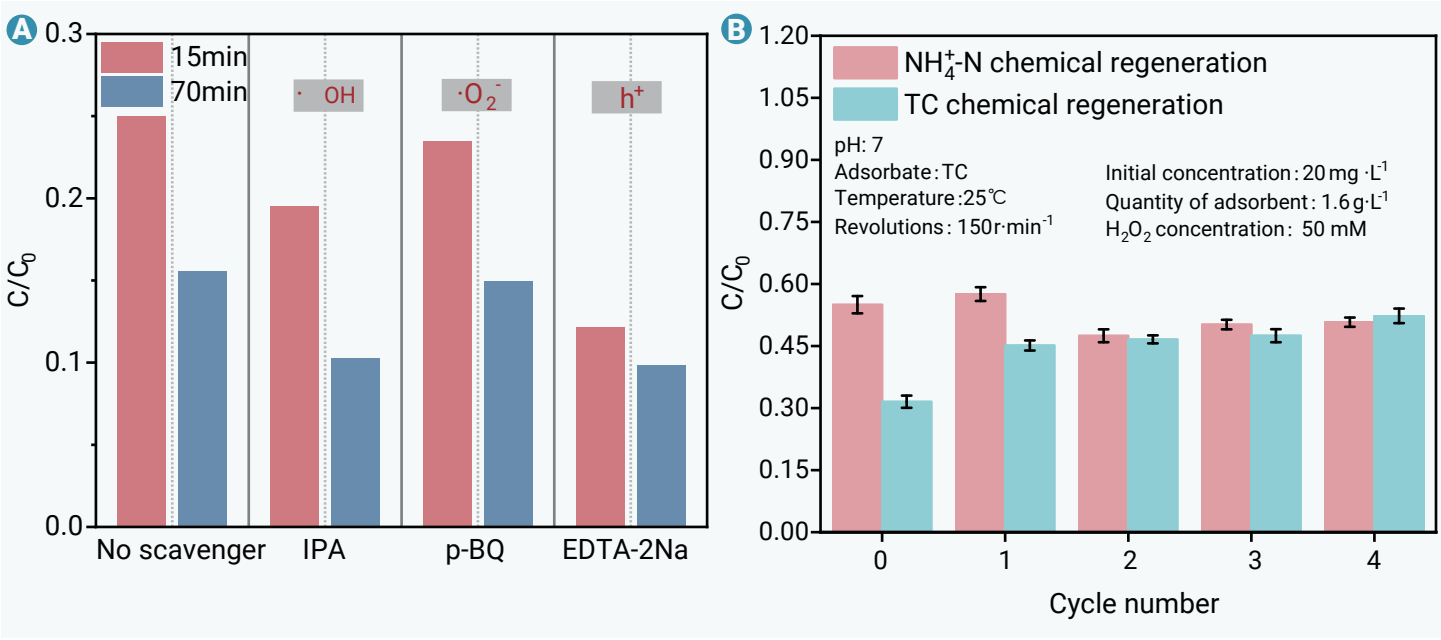


**Figure 7. (A) ROS quenching tests and (B) Removal performance of ammonia nitrogen and TC by 8% $MnFe_2O_4$/NaA after chemical regeneration (25 °C, pH=7.00, 75min, 50 mM $H_2O_2$, 20 mg·$L^{-1}$ $MnFe_2O_4$/NaA)**

Above values are summarised in Table 1, which also includes data from a variety of the most widely industry-used materials for comparison.

## Identification of Reactive Species and Mechanistic Insights

To clarify the main reactive species involved in the photocatalytic degradation of tetracycline (TC), radical-trapping experiments were performed under optimal conditions (pH 7, 50 mM $H_2O_2$, 1.6 g·$L^{-1}$ dosage). Specific scavengers were used: isopropanol (IPA) for hydroxyl radicals (·OH), p-benzoquinone (p-BQ) for superoxide radicals ($\cdot O_2^-$), and disodium ethylenediaminetetraacetate (EDTA-2Na) for holes ($h^+$). The results showed that IPA caused the greatest suppression of TC degradation, clearly indicating that photogenerated hydroxyl radicals are the main oxidative species. A significant inhibitory effect was also observed with p-BQ, confirming $\cdot O_2^-$ radicals as key secondary active species. In contrast, EDTA-2Na had a smaller effect, suggesting a lesser role for holes under these conditions. The ROS quenching tests (Figure 7A) indicate that ·OH and $\cdot O_2^-$ play dominant roles in TC removal.

## Recycling performance

Due to its inherent regenerability, the zeolite was chemically treated to desorb the adsorbed species, facilitating its reuse through multiple cycles. The post-use 8% $MnFe_2O_4$/NaA zeolite was placed in a 20 mL solution containing 1M HCl and 1M NaCl with a stirring speed of 150 r·$min^{-1}$ for 24 hours at room temperature. Subsequently, it was removed from the solution, rinsed with deionized water, and dried at 100°C for 2 hours before being utilized for the adsorption of ammonia nitrogen and the photocatalytic degradation of TC. The results, as depicted in Figure 7, indicate that even after four consecutive cycles, the zeolite was capable of maintaining a relatively good performance in terms of ammonia nitrogen adsorption and TC catalysis. Surprisingly, the ammonia nitrogen adsorption efficiency increased by approximately 4%, while the catalytic degradation of TC declined by around 21%. The improvement in ammonia nitrogen adsorption efficiency may be attributed to the regeneration process, which likely aided in the elimination of substances that may have obstructed or impeded the active sites during previous usage, consequently enhancing the adsorption capacity of the active sites for ammonia nitrogen. Furthermore, the regeneration process might have altered the surface properties of the zeolite, rendering it more favorable for the adsorption of ammonia nitrogen. Conversely, the marked reduction in tetracycline degradation efficiency observed over successive regeneration cycles is likely attributable to progressive mass loss of the $MnFe_2O_4$/NaA zeolite composite associated with repeated washing and drying procedures.

## CONCLUSION

In this study, a hydrothermal synthesis route was developed to convert

recycled coal fly ash into $MnFe_2O_4$/NaA composites, which demonstrated exceptional efficiency in both ammonia nitrogen adsorption and catalytic degradation of tetracycline (TC). Among the prepared samples, the 8% $MnFe_2O_4$/NaA zeolite demonstrated optimal performance, with a 51% adsorption rate for ammonia nitrogen and a 73% catalytic degradation rate for TC under conditions of 50 mM hydrogen peroxide concentration, 20 $mg{\cdot}L^{-1}$ initial TC concentration, and 1.6 $g{\cdot}L^{-1}$ dosage. These results underscore the excellent adsorption, photocatalytic degradation, and regenerative capabilities of $MnFe_2O_4$/NaA,[49] offering a novel and effective strategy for the treatment of water pollution containing ammonia nitrogen and antibiotics.[50]

## REFERENCES


1. Li C., Awasthi M.K., Liu J., et al. (2025). Veterinary tetracycline residues: Environmental occurrence, ecotoxicity, and degradation mechanism. *Environ. Res.* **266**:120417. DOI:10.1016/j.envres.2024.120417
2. Yang K., Yue Q., Kong J., et al. (2016). Microbial diversity in combined UAF–UBAF system with novel sludge and coal cinder ceramic fillers for tetracycline wastewater treatment. *Chem. Eng. J.* **285**:319. DOI:10.1016/j.cej.2015.10.019
3. Zhang H., Cheng S., Li B., et al. (2018). Fabrication of magnetic Co/BiFeO3 composite and its advanced treatment of pharmaceutical wastewater by activation of peroxysulphate. *Sep. Purif. Technol.* **202**:242. DOI:10.1016/j.seppur.2018.03.072
4. Daghrir R. and Drogui P. (2013). Tetracycline antibiotics in the environment: a review. *Environ. Chem. Lett.* **11**:209–227. DOI:10.1007/s10311-013-0404-8
5. Liu H., Yang L., Chen H., et al. (2023). Preparation of floating BiOCl0.6I0.4/ZnO photocatalyst and its inactivation of *Microcystis aeruginosa* under visible light. *J. Environ. Sci.* **125**:362. DOI:10.1016/j.jes.2021.12.044.
6. Zhang X., Li C., Chen T., et al. (2021). Enhanced visible-light-assisted peroxymonosulfate activation over MnFe2O4 modified g-C3N4/diatomite composite for bisphenol A degradation. *Int. J. Min. Sci. Technol.* **31**:1169. DOI:10.1016/j.ijmst.2021.11.008
7. Verraes C., Van Boxstael S., Van Meervenne E., et al. (2013). Antimicrobial resistance in the food chain: A review. *Int. J. Environ. Res. Public Health* **10**:2643–2670. DOI:10.3390/ijerph10072643
8. Kazmi R. and Chakraborty M. (2025). Use of coal mining wastes in the construction industry to promote a circular economy: a systematic literature review. *Circ. Econ. Sustain.* **5**:3593. DOI:10.1007/s43615-025-00551-1
9. Fernández-Pereira C., Leiva C., Luna-Galiano Y., et al. (2024). Improved recycling of a gasification fly ash: An integrated waste management approach within the framework of a circular economy. *Waste Manag.* **187**:31. DOI:10.1016/j.wasman.2024.06.029
10. Tang D., Pal M., Meng T., et al. (2025). Synthesis and applications of magnetic zeolites: A comprehensive review. *J. Supercond. Nov. Magn.* **38**. DOI:10.1007/s10948-025-06986-9.
11. Liu G., Lin Y., Zhang L., et al. (2024). Preparation of NaA zeolite molecular sieve based on solid waste fly ash by high-speed dispersion homogenization-assisted alkali fusion-hydrothermal method and its performance of ammonia-nitrogen adsorption. *J. Sci.: Adv. Mater. Devices* **9**:100673. DOI:10.1016/j.jsamd.2024.100673
12. Jankowska A., Panek R., Franus W., et al. (2024). Tailoring natural and fly ash-based zeolites surfaces for efficient 2,4-D herbicide adsorption: The role of hexadecyltrimethylammonium bromide modification. *Molecules* **29**. DOI:10.3390/molecules29225244.
13. Reed J.L.A., James A., Carey T., et al. (2024). Engineered species-selective ion-exchange in tuneable dual-phase zeolite composites. *Chem. Sci.* **15**:13699. DOI:10.1039/d4sc02664k
14. Munir N., Javaid A., Abideen Z., et al. (2023). The potential of zeolite nanocomposites in removing microplastics, ammonia, and trace metals from wastewater and their role in phytoremediation. *Environ. Sci. Pollut. Res.* **31**:1695. DOI:10.1007/s11356-023-31185-1
15. Wahba M.A. and Khaled R.K. (2025). V/Zn incorporated-MCM-41: Synthesis, characterization and visible light photocatalytic activity for tetracycline degradation. *J. Inorg. Organomet. Polym. Mater.* **35**:4445. DOI:10.1007/s10904-024-03533-2
16. Huang Kong E.D., Lai C.W., Juan J.C., et al. (2025). Recent advances in titanium dioxide bio-derived carbon photocatalysts for organic pollutant degradation in wastewater. *iScience* **28**. DOI:10.1016/j.isci.2025.112368.
17. Li J., Li Y., Xiong Z., et al. (2019). The electrochemical advanced oxidation processes coupling of oxidants for organic pollutants degradation: a mini-review. *Chin. Chem. Lett.* **30**:2139. DOI:10.1016/j.cclet.2019.04.057
18. Sawunyama L., Oyewo O.A., Makgato S.S., et al. (2025). TiO2–ZnO functionalized low-cost ceramic membranes from coal fly ash for the removal of tetracycline from water under visible light. *Discover Nano* **20**. DOI:10.1186/s11671-024-04178-3.
19. Shi J., Zhang M., Zhu L., et al. (2025). Recent advances in sustainable synthesis of zeolites. *Mater. Today Sustain.* **29**:101065. DOI:10.1016/j.mtsust.2024.101065
20. Zhou X., Liu S., Hu Y., et al. (2024). Green synthesis of porous bamboo-based activated carbon with high VOCs adsorption performance via steam activation method. *J. Porous Mater.* **31**:737. DOI:10.1007/s10934-024-01557-0
21. Bissenova M., Idrissov N., Kuspanov Z., et al. (2025). Hybrid adsorption–photocatalysis composites: a sustainable route for efficient water purification. *Mater. Renew. Sustain. Energy* **14**:44. DOI:10.1007/s40243-025-00319-5
22. Jiang Q., He J., Wang Y., et al. (2024). Efficient removal of ammonia–nitrogen in wastewater by zeolite molecular sieves prepared from coal fly ash. *Sci. Rep.* **14**. DOI:10.1038/s41598-024-72067-x.
23. Jalloul G., Hijazi N., Boyadjian C., et al. (2024). Titania-zeolite composite for tetracycline photocatalytic degradation under visible light: A comparison between doping and ion exchange. *Heliyon* **10**:e31854. DOI:10.1016/j.heliyon.2024.e31854
24. Bissenova M., Idrissov N., Kuspanov Z., et al. (2025). Hybrid adsorption–photocatalysis composites: a sustainable route for efficient water purification. *Mater. Renew. Sustain. Energy* **14**. DOI:10.1007/s40243-025-00319-5.
25. Liu Y., Wang L., Dai X., et al. (2024). Research on the adsorption-photocatalytic synergistic degradation of tetracycline by Au nanoparticles/TiO2 nanorods/biochar. *J. Alloys Compd.* **976**:172985. DOI:10.1016/j.jallcom.2023.172985
26. Ramu S., Kainthla I., Chandrappa L., et al. (2023). Recent advances in metal organic frameworks–based magnetic nanomaterials for waste water treatment. *Environ. Sci. Pollut. Res.* **31**:167. DOI:10.1007/s11356-023-31162-8
27. Derkaoui K., Bencherifa I., Elfiad A., et al. (2025). Unveiling the optical and dielectric properties of MnFe2O4: A high-performance visible-light photocatalyst for sustainable Rhodamine B degradation. *J. Electron. Mater.* **54**:5271. DOI:10.1007/s11664-025-11991-8
28. Tang D., Pal M., Meng T., et al. (2025). Synthesis and applications of magnetic zeolites: A comprehensive review. *J. Supercond. Nov. Magn.* **38**:146. DOI:10.1007/s10948-025-06986-9
29. Zhang T., Zhou T., He L., et al. (2020). Oxidative degradation of Rhodamine B by Ag@CuO nanocomposite activated persulfate. *Synth. Met.* **267**:116479. DOI:10.1016/j.synthmet.2020.116479
30. Wang Z., Lai C., Qin L., et al. (2020). ZIF-8-modified MnFe2O4 with high crystallinity and superior photo-Fenton catalytic activity by Zn-O-Fe structure for TC degradation. *Chem. Eng. J.* **392**:124851. DOI:10.1016/j.cej.2020.124851
31. Zhao W. and Yang B. (2024). Fabrication of magnetic MnFe2O4@HL composites with an in situ Fenton-like reaction for enhancing tetracycline degradation. *J. Colloid Interface Sci.* **658**:997. DOI:10.1016/j.jcis.2023.12.067
32. Jun B.-M., Elanchezhiyan S.S., Yoon Y., et al. (2020). Accelerated photocatalytic degradation of organic pollutants over carbonate-rich lanthanum-substituted zinc spinel ferrite assembled reduced graphene oxide by ultraviolet (UV)-activated persulfate. *Chem. Eng. J.* **393**:124733. DOI:10.1016/j.cej.2020.124733
33. Ghosh M., Akbar A. and Lakshmi M.B. (2024). Harnessing spinel ferrites: A comprehensive review of their role in water treatment. *ChemRxiv*. DOI:10.26434/chemrxiv-2024-hq04v.
34. Richard A.M., Tao D., Leclair C.A., et al. (2024). Analytical quality evaluation of the Tox21 compound library. *Chem. Res. Toxicol.* **38**:15. DOI:10.1021/acs.chemrestox.4c00330
35. Zheng A.L.T., Teo E.Y.L., Seenivasagam S., et al. (2024). Recent review on porous adsorbents for water decontamination: strategies for enhanced removal of tetracycline. *J. Porous Mater.* **32**:1. DOI:10.1007/s10934-024-01699-1
36. Liu G., Lin Y., Zhang L., et al. (2024). Preparation of NaA zeolite molecular sieve based on solid waste fly ash by high-speed dispersion homogenization-assisted alkali fusion-hydrothermal method and its performance of ammonia-nitrogen adsorption. *J. Sci. Adv. Mater. Devices* **9**:100673. DOI:10.1016/j.jsamd.2024.100673
37. Jiang X., Zhou Q. and Lian Y. (2023). Efficient photocatalytic degradation of tetracycline on the MnFe2O4/BGA composite under visible light. *Int. J. Mol. Sci.* **24**. DOI:10.3390/ijms24119378.
38. Shi J., Zhang M., Zhu L., et al. (2025). Recent advances in sustainable synthesis of zeolites. *Mater. Today Sustain.* **29**:101065. DOI:10.1016/j.mtsust.2024.101065
39. Jiang Q., He J., Wang Y., et al. (2024). Efficient removal of ammonia–nitrogen in wastewater by zeolite molecular sieves prepared from coal fly ash. *Sci. Rep.* **14**:21064. DOI:10.1038/s41598-024-72067-x
40. Lu A.-H., Salabas E.L. and Schüth F. (2007). Magnetic nanoparticles: Synthesis, protection, functionalization, and application. *Angew. Chem. Int. Ed.* **46**:1222–1244. DOI:10.1002/anie.200602866
41. Reddy L.H., Arias J.L., Nicolas J., et al. (2012). Magnetic nanoparticles: Design and characterization, toxicity and biocompatibility, pharmaceutical and biomedical applications. *Chem. Rev.* **112**:5818–5878. DOI:10.1021/cr300068p
42. Mohapatra J., Mitra A., Bahadur D., et al. (2013). Surface controlled synthesis of MFe2O4 (M = Mn, Fe, Co, Ni and Zn) nanoparticles and their magnetic characteristics. *Cryst. Eng. Comm.* **15**:524–532. DOI:10.1039/c2ce25957e
43. Cao K.L.A., Rahmatika A.M., Kitamoto Y., et al. (2021). Controllable synthesis of spherical carbon particles transition from dense to hollow structure derived from Kraft lignin. *J. Colloid Interface Sci.* **589**:252. DOI:10.1016/j.jcis.2020.12.077
44. Wang Z., Chen Q., Zhang J., et al. (2019). Characterization and source identification of tetracycline antibiotics in the drinking water sources of the lower Yangtze River. *J. Environ. Manage.* **244**:13. DOI:10.1016/j.jenvman.2019.04.070
45. Subasi B.S., Hayri-Senel T., Kahraman E., et al. (2025). Photocatalytic degradation of tetracycline from aqueous solution with graphene oxide and hydroxyapatite composites. *Sci. Rep.* **15**. DOI:10.1038/s41598-025-11502-z.
46. Zolekafeli Z., Sateria S.F., Mohamed A.H., et al. (2024). Removal of tetracycline using

tungsten disulfide/graphene oxide as photocatalyst: Effect of light irradiation and kinetic studies. *Bull. Chem. React. Eng. Catal.* **19**:512. DOI:10.9767/bcrec.20204
47. Kong Y., Zhuang Y., Han K., et al. (2020). Enhanced tetracycline adsorption using alginate-graphene-ZIF67 aerogel. *Colloids Surf. A Physicochem. Eng. Asp.* **588**:124360. DOI:10.1016/j.colsurfa.2019.124360
48. Sawunyama L., Oyewo O.A., Makgato S.S., et al. (2025). TiO2–ZnO functionalized low-cost ceramic membranes from coal fly ash for the removal of tetracycline from water under visible light. *Discover Nano* **20**:1. DOI:10.1186/s11671-024-04178-3
49. Nguyen H.A., Phuong N.T.T., Tran N.B., et al. (2025). Nano-enhanced Fenton/Fenton-like chemistry: integrating peroxidase nanozymes, MOFs, and MXenes for next-generation colorimetric biosensors. *Nanoscale Adv.* **7**:4763. DOI:10.1039/d5na00387c
50. Singh A., Pratap S.G. and Raj A. (2024). Occurrence and dissemination of antibiotics and antibiotic resistance in aquatic environment and its ecological implications: a review. *Environ. Sci. Pollut. Res.* **31**:47505. DOI:10.1007/s11356-024-34355-x

## FUNDING AND ACKNOWLEDGMENTS

This work was partially supported by the Zhejiang Provincial Natural Science Foundation (Key Project No. LZ22H300001), the Zhejiang Provincial Health Commission Foundation (Project Nos. 2024KY918, 2024ZL370), the 2022 Institution-specific Health Zhejiang Special Program of Hangzhou Medical College (Project No. YS2022008), the Medical Science and Technology Project of Zhejiang Province (Project No. 2025KY1030), the Innovation and Entrepreneurship Elite Project of Hangzhou Medical College's Humanity Entrepreneurship Education Fund, and the Basic Research Projects of Hangzhou Medical College (Project No. KYYB2023003).

## AUTHOR CONTRIBUTIONS

Y.S. : Conceptualization, Methodology, Formal Analysis, Data Curation, Visualization, Writing. B.X. : Conceptualization, Investigation, Formal Analysis, Data Curation, Validation, Writing. X.B. : Methodology，Investigation, Software, Validation, Visualization. Y.Y. : Investigation, Resources, Software. Q.Z. : Investigation, Formal Analysis, Validation. K.R. : Investigation, Visualization, Software. W.W. : Investigation, Data Curation, Validation. Y.Z. : Investigation, Resources, Visualization. S.Y. : Investigation, Formal Analysis, Software. S.H. : Investigation, Data Curation, Validation. Y.H. : Resources, Validation. D.J. : Review & Editing. Y.T. : Conceptualization, Methodology, Supervision, Project Administration, Funding Acquisition, Resources, Writing，Review & Editing, Corresponding Author. All authors contributed to the manuscript and approved the final version.

## DECLARATION OF INTERESTS

The authors declare no competing interests.

## ETHICAL STATEMENT AND PATIENT CONSENT

This work did not require ethical approval from a human subject or animal welfare committee.

## DATA AND CODE AVAILABILITY

The raw/processed data required to reproduce these findings cannot be shared at this time as the data also forms part of an ongoing study.